Mechanical compaction and strain localization in Bleurswiller sandstone

ARTICLE *in* JOURNAL OF GEOPHYSICAL RESEARCH: SOLID EARTH · AUGUST 2015

Impact Factor: 3.44 · DOI: 10.1002/2015JB012192

5 AUTHORS, INCLUDING:

Patrick Baud
University of Strasbourg
117 PUBLICATIONS **1,787** CITATIONS
SEE PROFILE

T. Reuschlé
Institut de Physique du globe de Strasbourg
53 PUBLICATIONS **568** CITATIONS
SEE PROFILE

Yuntao Ji
Institute of Geology, China Earthquake Admi…
13 PUBLICATIONS **22** CITATIONS
SEE PROFILE

Teng-fong Wong
Stony Brook University
165 PUBLICATIONS **6,058** CITATIONS
SEE PROFILE

AGU PUBLICATIONS

JGR

Journal of Geophysical Research: Solid Earth

RESEARCH ARTICLE
10.1002/2015JB012192

Key Points:
- Effective pressure law for sandstone
- Analysis of compaction band nucleation and propagation using CT
- Interpretation of the linear compactive envelope of Bleurswiller sandstone

Supporting Information:
- Supporting Information S1
- Table S1
- Table S2a
- Table S2b
- Figure S1
- Figure S2
- Figure S3

Correspondence to:
P. Baud,
patrick.baud@unistra.fr

Citation:
Baud, P., T. Reuschlé, Y. Ji, C. S. N. Cheung, and T.-f. Wong (2015), Mechanical compaction and strain localization in Bleurswiller sandstone, *J. Geophys. Res. Solid Earth*, *120*, doi:10.1002/2015JB012192.

Received 8 MAY 2015
Accepted 1 AUG 2015
Accepted article online 6 AUG 2015

Mechanical compaction and strain localization in Bleurswiller sandstone

Patrick Baud[1], Thierry Reuschlé[1], Yuntao Ji[2], Cecilia S. N. Cheung[3], and Teng-fong Wong[3,4]

[1]Institut de Physique du Globe de Strasbourg (UMR 7516 CNRS), EOST, Université de Strasbourg, Strasbourg, France, [2]State Key Laboratory of Earthquake Dynamics, Institute of Geology, China Earthquake Administration, Beijing, China, [3]Department of Geosciences, State University of New York, Stony Brook, New York, USA, [4]Earth System Science Programme, Faculty of Science, The Chinese University of Hong Kong, Hong Kong

Abstract We performed a systematic investigation of mechanical compaction and strain localization in Bleurswiller sandstone. Our data show that the effective pressure principle can be applied in both the brittle faulting and cataclastic flow regimes, with an effective pressure coefficient close to but somewhat less than 1. Under relatively high confinement, the samples typically fail by development of compaction bands. X-ray computed tomography (CT) was used to resolve preexisting porosity clusters, as well as the initiation and propagation of the compaction bands in deformed samples. Synthesis of the CT and microstructural data indicates that there is no casual relation between collapse of the porosity clusters in Bleurswiller sandstone and nucleation of the compaction bands. Instead, the collapsed porosity clusters may represent barriers for the propagation of compaction localization, rendering the compaction bands to propagate along relatively tortuous paths so as to avoid the porosity clusters. The diffuse and tortuous geometry of compaction bands results in permeability reduction that is significantly lower than that associated with compaction band formation in other porous sandstones. Our new data confirm that Bleurswiller sandstone stands out as the only porous sandstone associated with a compactive cap that is linear, and our CT and microstructural observation show that it is intimately related to collapse of the porosity clusters. We demonstrate that the anomalous linear caps and their slopes are in agreement with a micromechanical model based on the collapse of a spherical pore embedded in an elastic-plastic matrix that obeys the Coulomb failure criterion.

1. Introduction

In porous sandstone, the deformation, and strain may localize to develop compaction bands. These are tabular zones that have sustained inelastic compaction subperpendicular to their planar surfaces with negligible shear offset. With thicknesses on the order of 1–10 mm and trace lengths on the order of 1–10 m, compaction bands have been extensively investigated in two sandstone formations: Aztec sandstone in the Valley of Fire State Park, Nevada [*Hill*, 1989; *Sternlof et al*., 2005; *Eichhubl et al*., 2010], and Navajo sandstone at Buckskin Gulch adjacent to the East Kaibab monocline, Utah [*Mollema and Antonellini*, 1996; *Schultz et al*., 2010; *Fossen et al*., 2011].

Analogous to the field observations, laboratory studies have shown that compaction localization may develop in sandstones with porosities ranging from 13% to 28%, at stress states in the transitional regime between brittle faulting and cataclastic flow [*Wong et al*., 2001]. Such localization of compactant strain is associated with a broad spectrum of geometric complexity [*Baud et al*., 2004]. One end member is discrete compaction bands with typical thickness of ~2–3 grain diameters, which have been observed in sandstones with porosities in a range of 22–25% [*Klein et al*., 2001; *Baud et al*., 2004; *Fortin et al*., 2006; *Tembe et al*., 2008; *Townend et al*., 2008]. These discrete bands develop in the form of a subparallel array, accompanied by significant reduction of permeability [*Holcomb and Olsson*, 2003; *Vajdova et al*., 2004; *Baud et al*., 2012].

To our knowledge, there are three sandstones that have been observed to develop discrete compaction bands in the laboratory. One of the earliest investigations was conducted on Bentheim sandstone by *Klein et al*. [2001], who speculated that its relatively homogeneous mineralogy and well-sorted grains both promote the formation of compaction bands. The Aztec and Navajo sandstones, in which compaction bands are well documented in the field, are also predominately made up of quartz grains. However, subsequent laboratory studies on two other sandstones (Diemelstadt and Bleurswiller sandstones, with significant fractions of feldspars, oxides, and micas) show that discrete compaction bands develop in these sandstones as well [*Baud et al*., 2004; *Fortin et al*., 2006; *Louis et al*., 2006], even though their mineralogy is by no means

Table 1. Petrophysical Description of the Two Bleurswiller Sandstones Investigated in This Study

Sandstone name	Porosity (%)	Grain diameter (mm)	Composition
Bleurswiller1	25.2	0.224	quartz: 61%, feldspar 27%, clay 10.8%, mica 0.7%, oxides 0.5%
Bleurswiller2	24.2	0.200	quartz: 66%, feldspar 28%, clay 4%, mica 2%

homogeneous. These two are similar to Bentheim sandstone in porosity, but possibly due to the abundance of minerals other than quartz, their compactive yield stresses are lower by as much as a factor of 5 [*Tembe et al*., 2008].

Among the three, Bleurswiller sandstone has the lowest yield stress, and *Fortin et al*. [2006] have used acoustic emission (*AE*) location to elucidate its progressive development of discrete compaction bands. In their comparative studies of sandstones, *Tembe et al*. [2008] and *Cheung et al*. [2012] have also presented mechanical and microstructural data of Bleurswiller sandstone, in relation to the development of compaction localization and stress state. Nevertheless, there remain a number of intriguing questions on mechanical compaction and strain localization in this sandstone which remain unanswered.

First, the initiation of shear-enhanced compaction in Bleurswiller sandstone is anomalous, in that it is manifested by an approximately linear yield cap [*Fortin et al*., 2006; *Tembe et al*., 2008; *Cheung et al*., 2012]. Motivated by the experimental data and partly due to mathematical convenience, recent theoretical analyses of the development of kink folds [*Maillot and Leroy*, 2006; *Kampfer and Leroy*, 2009] have adopted such a linear cap, which can be parametrized simply in terms of a critical pressure P^* and a "compaction angle." This apparent linearity is in discrepancy with laboratory data of most porous sandstones, which show initial yield caps that are approximately elliptical [*Wong and Baud*, 2012]. One objective of this study is to investigate in more details the mechanical behavior of Bleurswiller sandstone and to identify the micromechanical processes responsible for the apparent anomaly in its compaction behavior.

Second, *Fortin et al*. [2006] reported preliminary X-ray computed tomography (CT) data, which indicated that their Bleurswiller sandstone samples had local clusters of anomalously high porosity, which seemed to collapse during the initial stage of inelastic compaction. Since these samples ultimately developed arrays of discrete compaction bands, a question naturally arises as to whether the bands had been triggered by stress perturbation related to collapse of the porosity clusters. Gaps in the CT and microstructural observations of *Fortin et al*. [2006] render it difficult to validate their hypothesis. Nevertheless, *Fossen et al*. [2011] have already gone ahead to adopt this hypothesis of "coalescence of pore collapse clusters" in their tectonic analysis of compaction bands in Navajo sandstone at Buckskin Gulch. Therefore, a second question we want to address is whether there is indeed a casual relation between compaction band formation and the initial collapse of porosity clusters in Bleurswiller sandstone. We performed systematic CT observations on several samples compacted to different stages; in particular, repeated CT measurements were made on one sample which was first scanned at the undeformed state and after each stage of deformation scanned again to monitor the evolution of damage and compaction localization.

The third question is related to permeability evolution. Unlike the other two sandstones which showed reduction of permeability by 2 orders of magnitude with the progressive development of compaction bands, the corresponding reduction (a factor of 2 to 5) in Bleurswiller sandstone was significantly smaller [*Fortin et al*., 2005]. The final objective of this study is to characterize the geometric attributes of compaction bands and elucidates the microstructural basis for this apparent discrepancy in permeability evolution.

2. Sample Material and Experimental Procedures

2.1. Sample Description

Bleurswiller sandstone is a grey arkosic arenite from the Vosges mountain in eastern France. Our samples were cored from two blocks with somewhat different mineralogy (Table 1). The first block (Bleurswiller1) is identical to that studied by *Fortin et al*. [2005, 2006] and *Tembe et al*. [2008]. The modal analysis is according to *Cheung et al*. [2012], who observed that *Fortin et al*. [2005] had underestimated the clay mineral fraction (10.8%) of clay. To assess whether mineralogy may have contributed to the anomalous behavior of this sandstone, we also investigated samples from a second block (Bleurswiller2) with a lower clay mineral fraction (4% [*Heap et al*., 2015]).

Our samples were cored perpendicular to the sedimentary bedding and then ground to obtain cylinders with diameter of 20.0 mm and length of 40.0 mm. Porosity of each sample was measured by water imbibition and the triple weight method. Initial porosities of the Bleurswiller1 samples used in this study ranged from 23.0% to 25.3% with a mean value of 24.3%. This is within the same range of the porosities of the samples reported in *Fortin et al*. [2005]. Initial porosities of the Bleurswiller2 samples ranged from 23.5% to 24.6% with a mean value of 24.2% (Table 1).

2.2. Experimental Methodology

The samples were first jacketed with a copper foil (of thickness 0.05 mm) and then with polyolefine tubing before being placed in the pressure vessel. All the experiments were performed at room temperature in the conventional triaxial configuration in the Strasbourg laboratory. In the wet experiments, samples were saturated with deionized water and deformed under fully drained conditions at pore pressures between 10 and 150 MPa. For the dry experiments, samples were dried in vacuum before deformation.

Confining pressure was regulated by a computer-controlled stepping motor connected to a pressure transducer with an accuracy of 0.05 MPa. Axial load was applied by a piston and regulated by a second computer-controlled stepping motor. Axial displacement was measured with an accuracy of 0.2 μm outside the pressure vessel, with a capacitive transducer mounted on the moving piston, which was servo-controlled to advance at a fixed rate (corresponding to a nominal strain rate of $1.0 \times 10^{-5}\,s^{-1}$). Pore volume change of a saturated sample was recorded by monitoring the displacement of the pore pressure generator with an angular encoder. Porosity change was then calculated as the ratio of the pore volume change to the initial bulk volume of the sample. In a dry test, volumetric strain was recorded by monitoring the piston displacement of the confining pressure generator with an angular encoder. The detailed methodology was described by *Baud et al*. [2009].

For investigation of permeability of a triaxially compressed sample, we used the steady state flow technique. Special endcaps were designed to enable fluid flow through the sample. A difference of 0.5 MPa in pore pressure between the upstream and downstream sides of the system was maintained by flow through a small leakage on the downstream side (at atmospheric pressure). The cumulative discharge was measured with a precision balance, corrected for loss by water evaporation. Permeability was then determined directly using Darcy's law.

2.3. X-ray Microcomputed Tomography and Microstructural Analysis

X-ray CT imaging was performed on selected samples at the High-Resolution CT Facility at the University of Texas at Austin, following procedures detailed by *Ketcham and Carlson* [2001] and *Louis et al*. [2006]. The voxel size was $49 \times 49 \times 49\,\mu m^3$. The reconstructed image comprises 416 slices, each of which is made up of 432×892 voxels.

After acquisition of the CT images, the failed samples were impregnated with epoxy and then sawed along a plane-parallel to the axial direction to prepare petrographic thin sections. Optical microscopy was performed using a Nikon polarizing microscope. Thin sections were sputter coated with 3 nm of gold for scanning electron microscope (SEM) imaging, performed at Stony Brook University using a LEO 1550 microscope under backscattered electron mode at a voltage up to 10 kV.

3. Mechanical Deformation and Permeability Evolution

We adopt the convention that compressive stresses and compactive strains (i.e., shortening and porosity decrease) are positive. The maximum and minimum principal compressive stresses are denoted by σ_1 and σ_3, respectively. The differential stress is defined to be $\sigma_1 - \sigma_3$, and the pore pressure is denoted by P_p. Following *Paterson and Wong* [2005], the difference between the confining pressure (P_c) and pore pressure will be referred to as the conventional effective pressure (P_{eff}). If there is no ambiguity in the context, we often refer to this quantity as simply the effective pressure, and likewise $(\sigma_1 + 2\sigma_3)/3 - P_p$ as the effective mean stress.

Altogether we conducted six series of experiments in this study:

1. To complement the data set of *Tembe et al*. [2008], six triaxial experiments on saturated Bleurswiller1 samples were conducted at effective pressures ranging from 10 to 100 MPa (Table S1 in the supporting information). The pore pressures in these tests were fixed at 10 MPa. The data allow us to better characterize the compactive cap and brittle-ductile transition.

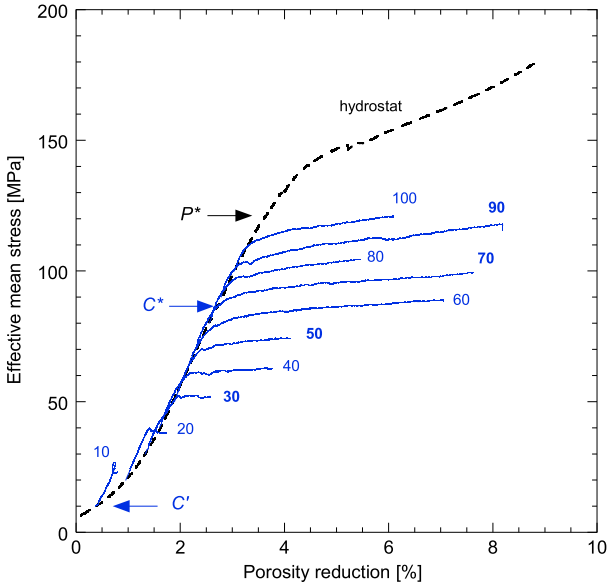

Figure 1. Representative mechanical data for triaxial compression experiments on saturated Bleurswiller1 sandstone deformed at conventional effective pressures ranging from 10 to 100 MPa. Effective mean stress is plotted as a function porosity reduction. The effective pressure is indicated on each curve, in bold for new experiments performed in this study. The other experiments were previously presented in *Tembe et al.* [2008]. For reference, the hydrostatic data are shown as a dashed curve. The arrows indicate the critical pressures *C'*, *C**, and *P**.

2. To study the effect of water weakening, we performed triaxial tests on three dry Bleurswiller1 samples at confining pressures ranging from 30 to 80 MPa (Table S1).
3. Sixty-two triaxial and 1 hydrostatic tests were performed on saturated Bleurswiller2 samples (Table S2). To investigate the effective stress behavior of mechanical compaction, these tests were conducted at pore pressures fixed at one of six values (0.5, 10, 50, 75, 100, or 150 MPa).
4. To further study the effect of water weakening, we performed triaxial tests on 16 dry Bleurswiller2 samples at confining pressures ranging from 5 to 140 MPa (Table S2).
5. A triaxial experiment was performed on a Bleurswiller2 sample (at an effective pressure of 80 MPa) to determine the evolution of permeability with differential stress.
6. Four triaxial compression experiments were performed on three saturated Bleurswiller1 samples in relation to CT imaging. Two samples were deformed to relatively large strains (~3%) at effective pressures of 40 MPa and 80 MPa, respectively. These samples have developed compaction bands and were scanned afterward. The third sample was scanned three times: first in the undeformed state, and then after it had been deformed at effective pressure of 80 MPa to just beyond compactive yield, and finally after it had attained a cumulative strain of ~1.5%.

3.1. Dilatant Faulting and Shear-Enhanced Compaction

Mechanical data for dry and wet samples of Bleurswiller1 and Bleurswiller2 samples are qualitatively similar. We will illustrate the overall behavior with reference to the wet Bleurswiller1 samples. Our new data together with those of *Tembe et al.* [2008] represent a comprehensive set of mechanical data (Table S1) at effective pressures ranging from 0.1 MPa to 100 MPa. We plot in Figure 1 the effective mean stress as a function of porosity reduction for 10 selected experiments ranging in effective pressure from 10 to 100 MPa. For reference the hydrostatic compression data of a saturated sample are shown as the dashed curve, with the inflection point *P** corresponding to the critical pressure for onset of grain crushing and pore collapse [*Zhang et al.*, 1990].

In a conventional triaxial experiment, if the axial stress increases by an increment $\Delta\sigma_1$, then the mean stress would also increase by $\Delta\sigma_1/3$. This stress increment induces a porosity change which comprises elastic and possibly inelastic components. In the poroelastic regime, the inelastic component is absent, and therefore, the porosity change is controlled solely by the mean stress, which would require the triaxial data to coincide with the hydrostat in Figure 1. In contrast, with the onset of inelasticity there is appreciable deviation from the hydrostat, because the porosity change in a triaxial compression experiment would then depend on not only the mean stress but also on the deviatoric stress. Accordingly, the triaxial data for effective mean stress as a function of porosity change would initially coincide with the hydrostat in the poroelastic regime up to a critical stress state (marked as *C'* or *C** in Figure 1), beyond which there was an accelerated increase or decrease in porosity in comparison with the hydrostat. These accelerated porosity changes represent inelastic dilatation or compaction induced by the deviatoric stress field. In our saturated Bleurswiller1 samples, dilatancy was observed only in the sample deformed at P_{eff} = 10 MPa. Beyond dilatancy, this sample ultimately failed by brittle faulting. In the other nine samples the inelastic deformation was compactive (Figure 1), and this phenomenon is

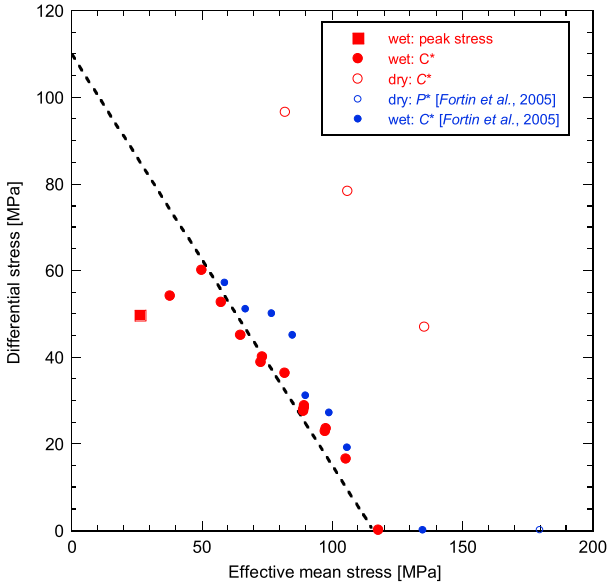

Figure 2. Strength envelopes for Bleurswiller1 sandstone (red) as described by the peak stress (square) and the onset of shear-enhanced compaction C^*(circles). Data on dry and wet samples are presented as open and close symbols, respectively. The data of *Fortin et al.* [2005] on the same rock are also presented as blue symbols. The straight line predicted by the model of *Zhu et al.* [2010] with slope of −0.95 is also given for reference.

referred to as "shear-enhanced compaction" [*Wong et al.*, 1997]. These samples typically failed by development of shear and/or compaction bands.

3.2. Critical Stresses for Brittle Faulting and Compactive yield: Linear Envelopes and Water Weakening

From the mechanical data we determined the brittle strength and yield stresses C^* for the onset of shear-enhanced compaction (Table S1). For comparison, data of *Fortin et al.* [2006] are also shown in Figure 2a. The brittle strength data map out a linear envelope typical of Coulomb failure, with a positive slope comparable to other porous sandstones [*Wong and Baud*, 2012]. For compactive yield, data from three different studies are consistent in that they all fall on an approximately linear cap with a slope of about −1. Such a linear cap is atypical of porous sandstones, which are commonly associated with an elliptical cap [*Wong and Baud*, 2012].

Since the mechanical behavior of the dry Bleurswiller1 samples in experiment series (2) was qualitatively similar, the compactive yield stress C^* can be determined analogously (Table S1 and Figure 2a). Comparison of the dry and wet data indicate that in the wet samples, onset of shear-enhanced compaction developed at stresses significantly lower than the dry samples, likely related to weakening in the presence of water similar to that observed in other porous sandstones [*Baud et al.*, 2000]. However, the yield caps of dry and wet samples both follow linear trends, with similar slopes of about −1. This implies that linearity of the yield cap is not due to the presence of water, but likely related to either the pore structure or mineralogy of Bleurswiller sandstone.

3.3. Critical Stresses for Brittle Faulting and Compactive Yield: Effect of Pore Pressure

Data from experiment series (3) on Bleurswiller2 samples allow us to clarify the effective stress behavior associated with brittle faulting and compactive yield. If the poromechanical response to an applied stress σ_{ij} and pore pressure P_p coincides with that to the stress difference $\sigma_{ij} - \alpha P_p \delta_{ij}$, then the latter quantity is referred to as the "effective stress." In particular, if the coefficient α is unity, then the quantity $\sigma_{ij} - P_p \delta_{ij}$ corresponds to Terzaghi's formulation, which we will call "conventional effective stress" here.

We will first consider the brittle faulting data. Twelve experiments were conducted at a fixed pore pressure of 0.5, 10, 50, 75, 100, or 150 MPa and conventional effective pressure of 0.5, 5, or 10 MPa. Representative data for a conventional effective pressure of 10 MPa are presented in Figure 3a. The mechanical responses of these samples are similar in that they all showed strain softening and brittle failure. For the pressure range investigated, the brittle strength data fall on a linear trend. Data for the peak stress show an overall trend for the samples deformed at higher pore pressures to have somewhat higher strengths, which suggests that the use of the conventional effective stress (Figure 3a) would overestimate the effect of pore pressure on strength reduction and that the coefficient α may actually be less than 1. In Figures 3b and 3c, we plot the brittle strength as a function of either $P_c - P_p$ or $P_c - 0.945\ P_p$, and it can seen that the latter can be fitted reasonably well with a linear Coulomb envelope. The effective stress coefficient $\alpha = 0.945$ was estimated by regression analysis of the brittle strength data assuming a linear envelope. One may speculate this pore pressure effect arises because the deformation was not fully drained and might involve dilatancy hardening [*Brace and Martin*, 1968]. However, we consider this unlikely for two reasons. First, the hardening behavior

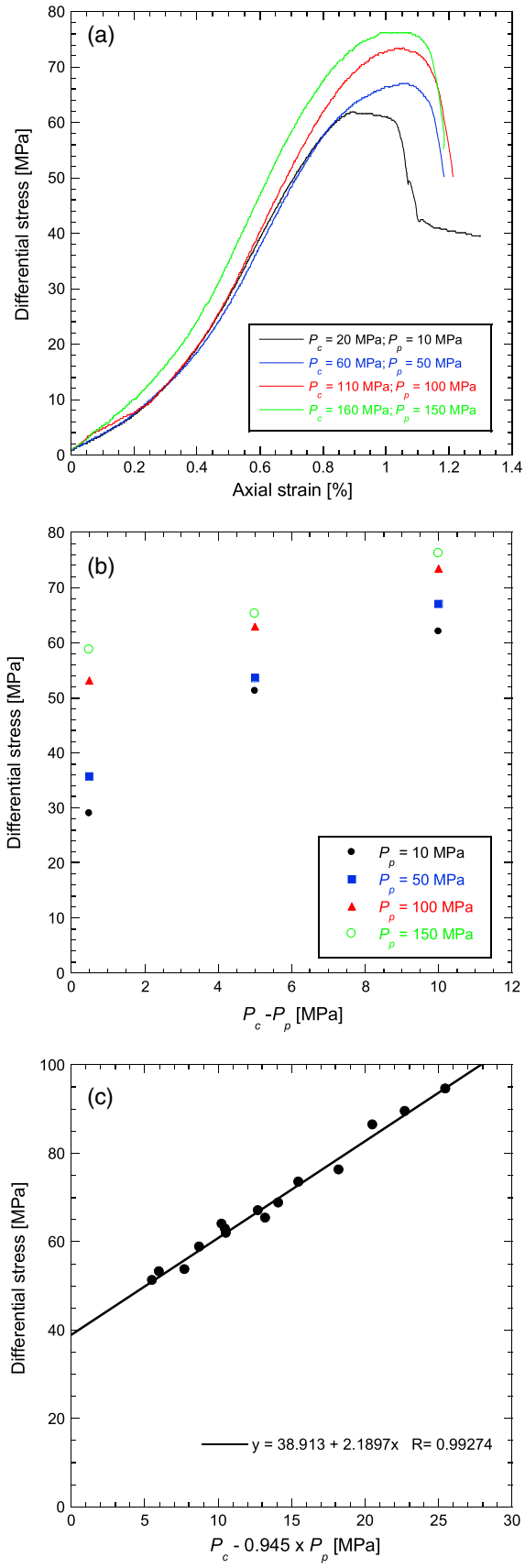

seemed not to have any systematic dependence on pore pressure. Second, *Heap et al.* [2015] showed that the permeability of Bleurswiller sandstone is 8.5×10^{-13} m^2, which is considered to be sufficiently high for the effective drainage at the strain rate used in our experiments.

We next consider compactive yield. Twenty-six experiments were conducted at a fixed pore pressure of 10, 50, or 100 MPa and fixed effective pressure ranging from 20 to 90 MPa. These samples all showed shear-enhanced compaction and failed by development of shear and/or compaction bands. The mechanical responses of these samples show slight deviation from Terzaghi's effective stress principle. This is illustrated by the data for conventional effective pressure of 50 MPa (Figure 4a), and the slight difference between data at different pore pressures suggests an effective stress coefficient that is equal to or somewhat less than 1. The data for effective mean stress as a function of porosity change are similar to Figure 1, such that we can identify from the curves the yield stresses C^* for the onset of shear-enhanced compaction, which are plotted in Figure 4b. The effective stress coefficient $\alpha = 0.96$ was estimated by regression analysis of the compactive yield data assuming a linear cap.

Mechanical behavior of the dry Bleurswiller2 samples in experiment series (4) was qualitatively similar (Figure 4c). Comparison of the brittle strength and compactive yield stresses with the wet data from series (3) indicates that both brittle failure and onset of shear-enhanced compaction in the wet samples developed at stresses significantly lower than the dry samples.

Figure 3. (a) Representative brittle data for Bleurswiller2. Differential stress is presented as a function axial strain for a conventional effective pressure of 10 MPa and four pore pressures. (b) Brittle failure envelopes for the same pore pressures. Differential stress is plotted as a function of conventional effective pressure ($\alpha = 1$). (c) Same plot for $P_{\text{eff}} = P_c - 0.945\ P_p$.

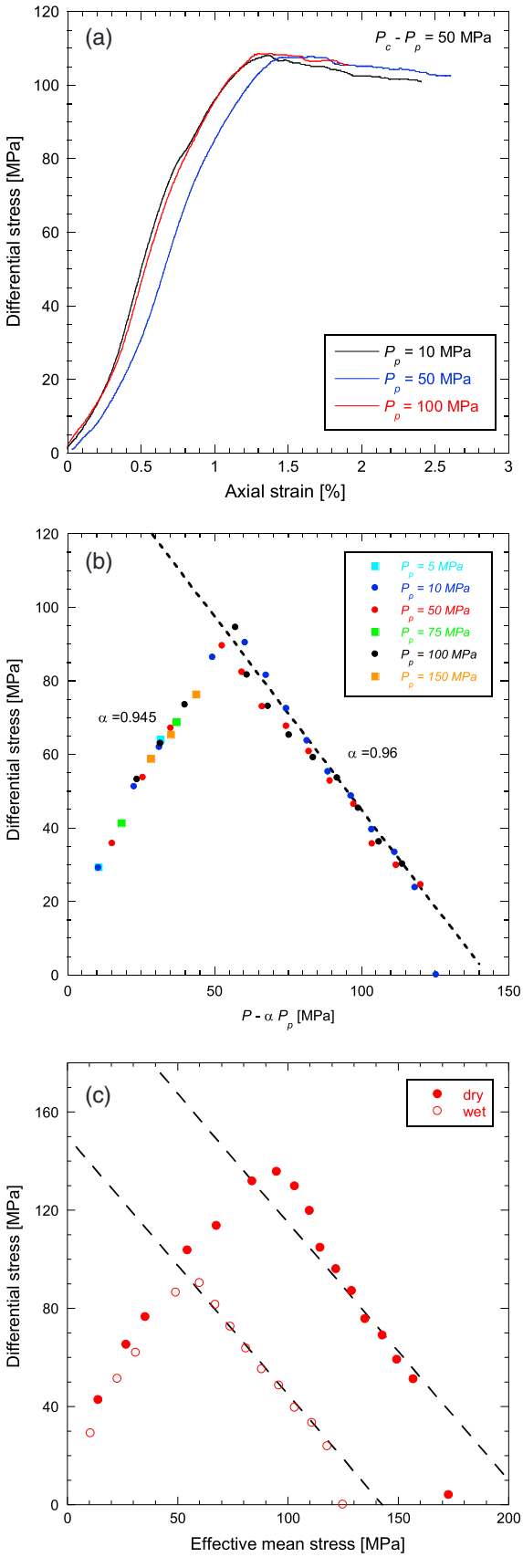

Nevertheless, the yield caps of the dry and wet samples both follow linear trends with comparable slopes. It can be also seen in Figure 4c that in both dry and wet conditions the critical pressure P^* is not exactly on these linear compactive envelopes but a bit lower. We cannot rule out the possibility that the cap becomes almost vertical in the vicinity of P^*. However, it should be noted that *Heap et al.* [2015] showed recently that significant time-dependent compaction can occur at relatively high effective pressures in Bleurswiller sandstone. Because our hydrostatic experiments, unlike the triaxial ones, were performed in pressure control (and not at constant strain rate), increasing the confining pressure in small steps to reach the onset of grain crushing and pore collapse, it is not impossible that these data somehow include some minor time-dependent component. Our P^* values should therefore be considered as lower bounds for the onset of grain crushing and would probably be much closer to the linear envelopes at higher strain rates.

Notwithstanding the similarities, there are two differences between the blocks. First, although the compactive yield caps of wet and dry Bleurswiller2 have slopes close to 1, they are somewhat steeper than those of Bleurswiller1. Second, the brittle strengths and compactive yield stresses for Bleurswiller2 samples are significantly higher. This discrepancy is probably related to the

Figure 4. (a) Mechanical data on Bleurswiller2 sandstone, differential stress versus axial strain, for a conventional effective pressure of 50 MPa, and pore pressures of 10, 50, and 100 MPa. (b) Strength envelopes for Bleurswiller2 sandstone for different pore pressures: differential stress as a function of effective mean stress. The effective pressure coefficients were 0.945 and 0.96, for the brittle and compactant regimes, respectively. (c) Comparison of dry (open circles) and wet (closed circles) data for Bleurswiller2 sandstone: differential stress versus conventional effective mean stress ($\alpha = 1$). The straight line predicted by the model of *Zhu et al.* [2010] with slope of −1.05 is also given for reference.

difference in modal composition. Bleurswiller2 samples have significantly higher percentage of quartz and less clay (Table 1). It is of interest to note that the modal composition of Bleurswiller2 is very similar to that of Diemelstadt sandstone, which can fail also by compaction band formation [*Tembe et al.*, 2008]. Whereas Diemelstadt sandstone and most other porous sandstones have compactive yield caps that are approximately elliptical [*Wong and Baud*, 2012], the corresponding caps for both Bleurswiller1 and Bleurswiller2 sandstone are linear. Hence, our data suggest that we can rule out mineralogy as an important factor for the discrepancy in the shape of the cap, and the anomalously linear behavior of Bleurswiller sandstone is more likely related to its pore structure.

3.4. Failure Modes

The exterior appearance of failed Bleurswiller2 samples (Figure 5a) indicates a progressive transition in failure mode with increasing effective pressure. Shear bands at angles of ~30° (relative to σ_1) have developed in the two samples deformed at conventional effective pressures of 10 MPa and 20 MPa. With increase in confinement, conjugate sets of high-angle shear bands can be seen in the three samples deformed at effective pressures between 30 and 50 MPa. At even higher confinement (70 and 90 MPa), a mixed mode of high-angle shear bands and tortuous compaction bands subperpendicular to σ_1 can be observed. Exterior appearance of these Bleurswiller2 samples is qualitatively similar to Bleurswiller1 samples as reported by *Fortin et al.* [2005].

We also studied petrographic thin sections of the failed Bleurswiller1 samples. Figure 5b presents micrographs of the samples that failed at effective pressures ranging from 20 to 100 MPa. Dotted lines were used to highlight the strain localization features, which indicate a progressive transition in failure mode with increasing effective pressure. A synthesis of the exterior appearance and optical microscope observations would suggest that geometric attributes of strain localization in these failed samples can be quite complex. The geometric complexity imaged by CT will be discussed in a latter section.

For selected Bleurswiller1 samples, we also counted the number of compaction bands that appear in the thin section to have cut through the sample. It is difficult to uniquely determine the number of discrete compaction bands because of their somewhat tortuous character and tendency to merge and crosscut one another. Following the approach used by *Vajdova et al.* [2004], we set up an array of three test lines through every thin section in the axial direction (two near the sides and one in the middle) and count the number of intersections of the compaction bands with each test line. The number of bands n is the arithmetic mean of these three values. Similar to the data of *Vajdova et al.* [2004] for Bentheim sandstone, there is an approximately linear trend for the number of bands to increase with accumulated inelastic strain (Figure 6). However, there are significantly fewer bands in Bleurswiller1 samples; at the same strain value, number of compaction bands here is only about half of that in Bentheim sandstone.

3.5. Permeability Evolution

In experiment series (5), permeability of a Bleurswiller2 sample as function of differential stress and axial strain was determined at effective pressure of 80 MPa (Figure 7). We estimated shear-enhanced compaction in this sample to have initiated at a strain of 0.42%, beyond which we observed an appreciable decrease in permeability by an order of magnitude with further accumulation of strain. The permeability evolution here is similar to that in three Bleurswiller1 samples reported by *Fortin et al.* [2005], with two notable differences. First, the permeability decrease (by a factor of ~2–5) observed in this other block was somewhat less. Second, the permeability values (on the order of 10^{-14} m^2) in these samples are significantly lower. The discrepancy can probably be attributed to mineralogical differences, in that the higher clay mineral content in Bleurswiller1 sandstone is expected to decrease the permeability. It should also be noted that the permeability reductions of 1 order of magnitude or less in Bleurswiller sandstone are significantly lower than reductions by 2–3 orders of magnitude typically observed in Bentheim [*Vajdova et al.*, 2004] and Diemelstadt [*Baud et al.*, 2012] sandstones.

4. Microstructural Observations and X-ray Microcomputed Tomography

4.1. Mineralogy and Pore Space Heterogeneity

As noted by *Fortin et al.* [2005], Bleurswiller sandstone has a heterogeneous pore space, with a number of "porosity clusters" embedded in a relatively homogeneous matrix, which comprises well-cemented grains

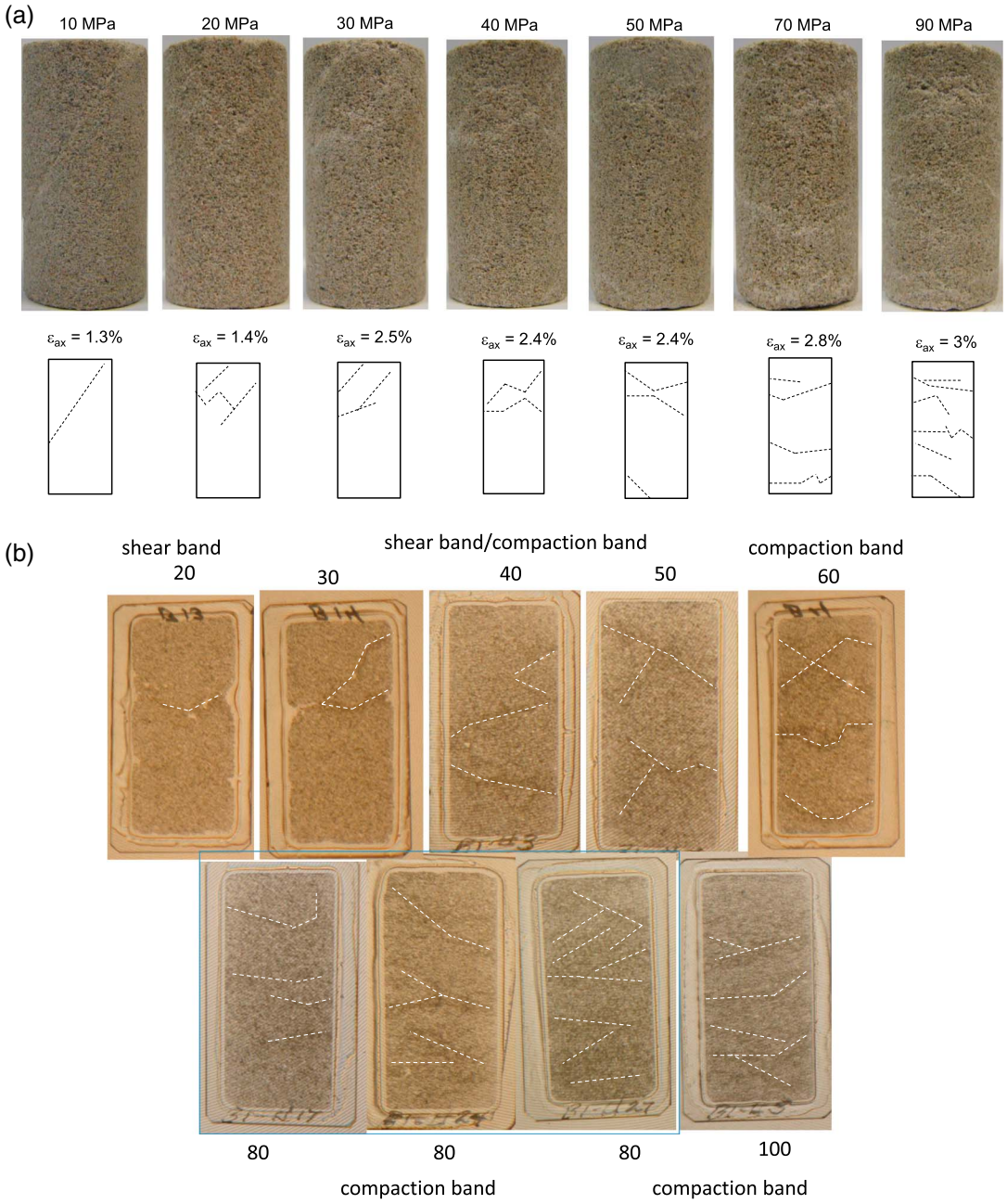

Figure 5. (a) Series of photographs picturing the samples of Bleurswiller2 sandstone deformed in wet conditions at different effective pressures. (b) Transmission optical micrographs of deformed Bleurswiller1 sandstone samples deformed in wet conditions. The conventional effective pressure and the level of axial strain are indicated next to the thin sections. The width of each thin section is ~20 mm. Principal stress σ_1 was along the axial direction.

of primarily quartz, as well as feldspar and clay. The grains in this matrix are well sorted [*Cheung et al.*, 2012], and the interstitial pores are fairly uniform in size (Figure 8a). In contrast, the porosity clusters are made up of poorly sorted grains connected in what appears to be a rather open structure (Figure 8b). Many of the grains are barely in contact with their nearest neighbors, and the cluster seems ready to collapse in response to a slight stress perturbation. It is beyond the scope of this study to explore the diagenetic process that resulted in these clusters. One possibility is that they correspond to localized zones of enhanced weathering or initially to clusters of more soluble grains. Although the micrographs are from a Bleurswiller1 sample, our observations indicate that similar features are also present in Bleurswiller2 samples. Although the clay fraction is lower, analogous heterogeneities in the form of porosity clusters are found in this other block.

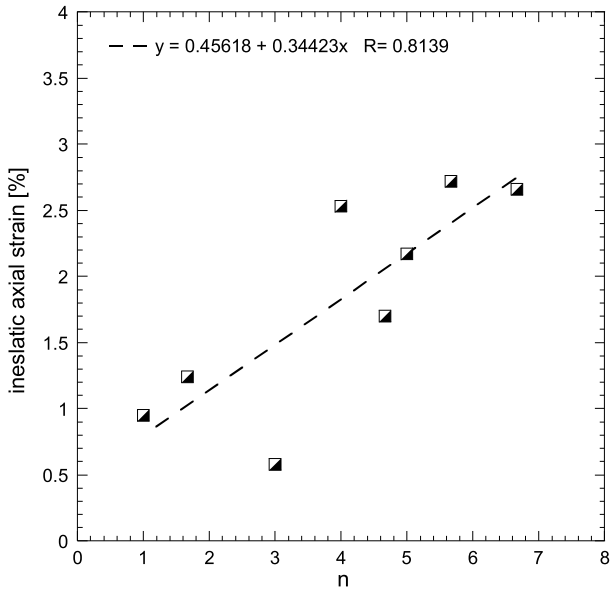

Figure 6. Axial inelastic strain as a function of number of compaction bands for wet samples of Bleurswiller1 sandstone deformed at effective pressures between 20 and 100 MPa.

CT imaging was used to characterize these heterogeneities in a Bleurswiller1 sample (Bl28). Porosity clusters correspond to darker areas (with relatively low grey levels) that can be visually recognized on a 2-D section of the tomograph (Figure 9a). To a first approximation the CT attenuation coefficient and its corresponding grey level are linearly related to the density. Since we know the density of the sandstone sample and average grey level of its CT image, as well as the corresponding values for air, these two data points define a straight line on a plot of grey level versus density, which we can then use to infer the local density from grey level (Figure 9b). Since there is only slight variation in density among the sandstone grains, we can assume a constant grain density such that local density of the porous aggregate decreases linearly with porosity. Accordingly, the linear calibration can also be used to infer local porosity from grey level. We evaluated the average grey levels of voxels enclosed in four darker areas and two lighter areas in Figure 9a and used the linear calibration to infer their local porosities. On this 2-D section, the porosity clusters 1–4 have grey levels $>$21,750, corresponding to local porosities that exceed the mean porosity by 10% or more (Figure 9b).

To visualize the spatial distribution of these porosity clusters in 3-D, we first binarized the CT image using a threshold grey level of 23,280. Voxels with grey levels below this threshold are shown in blue, which corresponds to a local porosity greater than ~39%. (Figure 9c). In the binarized image, we counted a total of 84,511 isolated blobs made up of interconnected blue voxels. According to our observations (Figures 8a and 8b), a porosity cluster is made up of relatively large nodal pores connected by throats, which have lateral dimensions significantly wider than the other throats in the matrix region exterior to the cluster. To eliminate these relatively narrow throats in the matrix and at the same time preserve the wider throats inside the porosity clusters, we applied morphological opening, an operation that first applies erosion with a structuring element (a cube with 5^3 voxels) followed by dilation. This morphological process significantly reduced the number of blobs to 5115. Based on our systematic comparison of the blob geometry with microstructural observations, we concluded that only the largest 28 blobs (with volume greater than 2.2 mm^3) correspond to the preexisting porosity clusters. To help visualize an individual cluster, we enclosed the voxels with their convex hull (Figure 9d), defined to be the convex surface with the minimum volume that

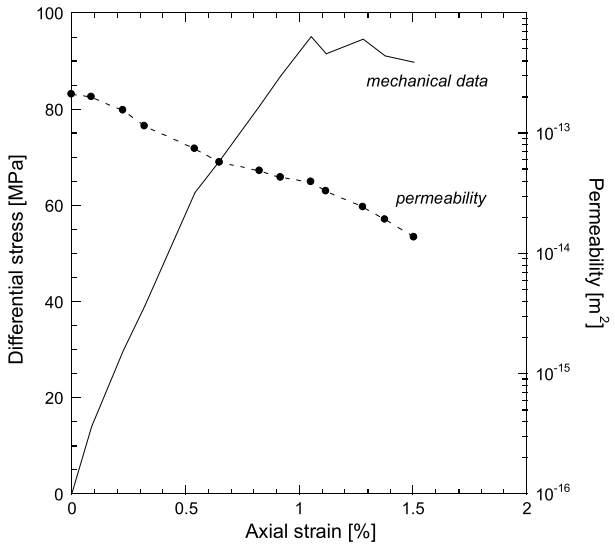

Figure 7. Differential stress and permeability as a function of axial strain for a triaxial permeability experiments performed on a Bleurswiller2 sandstone sample (B110) at an effective pressure of 80 MPa.

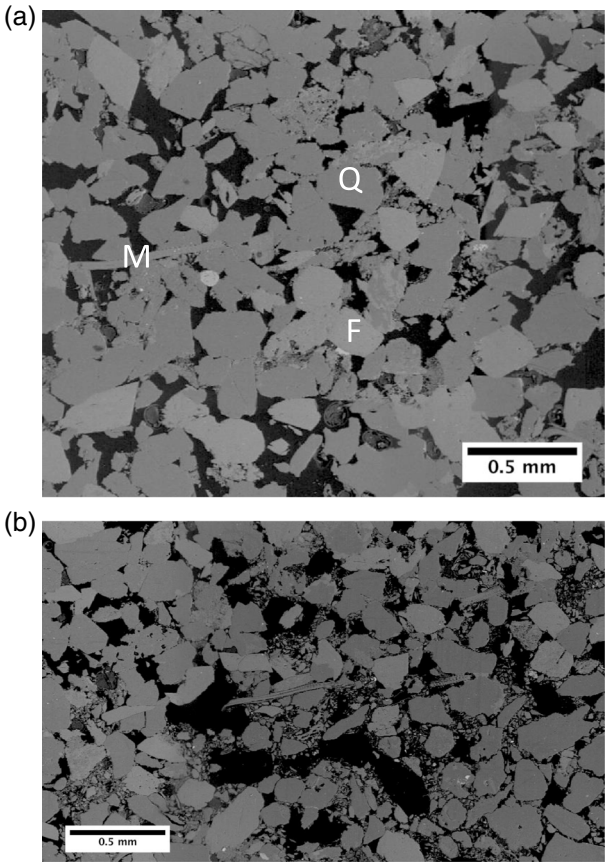

Figure 8. Backscattered scanning electron micrographs of Bleurswiller1 sandstone that shows (a) intact mineralogy consisting of quartz (*Q*), feldspar (*F*), and mica (*M*). (b) Local cluster of anomalously high porosity (dark).

can wrap around and enclose all the voxels [*Gonzalez and Woods*, 2008].

4.2. CT Imaging of Compaction Bands

Our experimental data on differential stress as a function of axial strain for the four experiments in series (6) are presented in Figure 10. These tests were all conducted at pore pressure of 10 MPa. To visualize strain localization features in CT images, we adopted the technique of *Louis et al*. [2006], which assumes that grain crushing in a clastic material would homogenize the spatial distribution of X-ray attenuation [*Otani et al*., 2005], and accordingly, the relative dispersion provides a proxy for the local damage intensity. Hence, a zone of relatively low dispersion would likely arise from cataclastic strain localization. This technique has been successfully applied to delineate compacting shear bands and compaction bands in porous sandstones [*Louis et al*., 2006; *Charalampidou et al*., 2011, 2013].

Guided by preliminary analyses using a range of values for the elemental volume, we finally settled on an elemental volume that is made up of 19^3 voxels. The X-ray measurement provided an ensemble of 6859 CT values for each elemental volume. We then evaluated the mean value μ and standard deviation σ of this ensemble, as well as coefficient of variation ($\delta = \sigma/\mu$). Once evaluated, the elemental volume was shifted in one of the three directions by one voxel, and the calculation repeated. Deformation bands correspond to localized zones associated with intense cataclastic damage and relatively low δ value in a CT image.

In Figures 11 and 12, we present selected serial sections orthogonal to the axes of samples Bl24 and Bl3, respectively. To achieve a sufficiently wide dynamic range for displaying the data, we have normalized and shifted the scale for the coefficient of variation δ, so that the minimum and maximum values in a sample correspond to 0 and 1, respectively. In these two samples intense damage has localized in many sections. In particular, several sections of Bl24 have pervasive damage. To highlight the damage distribution in 3-D, we binarized the image by applying a threshold value of 0.5 to the normalized coefficient of variation and present in Figures S1 and S2 in the supporting information videos that show the samples Bl24 and Bl3 rotating over 360°. A voxel with normalized coefficients between 0 and 0.5 is shown in blue, considered to be a proxy for intense damage. The damage in this binarized image is interconnected in a geometrically complex pattern to constitute multiple strands of compaction bands subperpendicular to the maximum principal stress σ_1. These bands seem more diffuse and tortuous in comparison to similar bands imaged in Diemelstadt sandstone by *Louis et al*. [2006].

After the CT images had been acquired, thin section were prepared from the deformed samples and SEM observations conducted to probe the grain-scale microstructure, particularly in areas of intense damage inferred from the CT images. We present here observations on three such areas within compaction bands. A compaction band ~1 mm wide in sample Bl3 can be seen near the midsection of Figure 13a. Pervasive grain crushing had basically eliminated all the larger pores within the band, whereas grains and pores above and

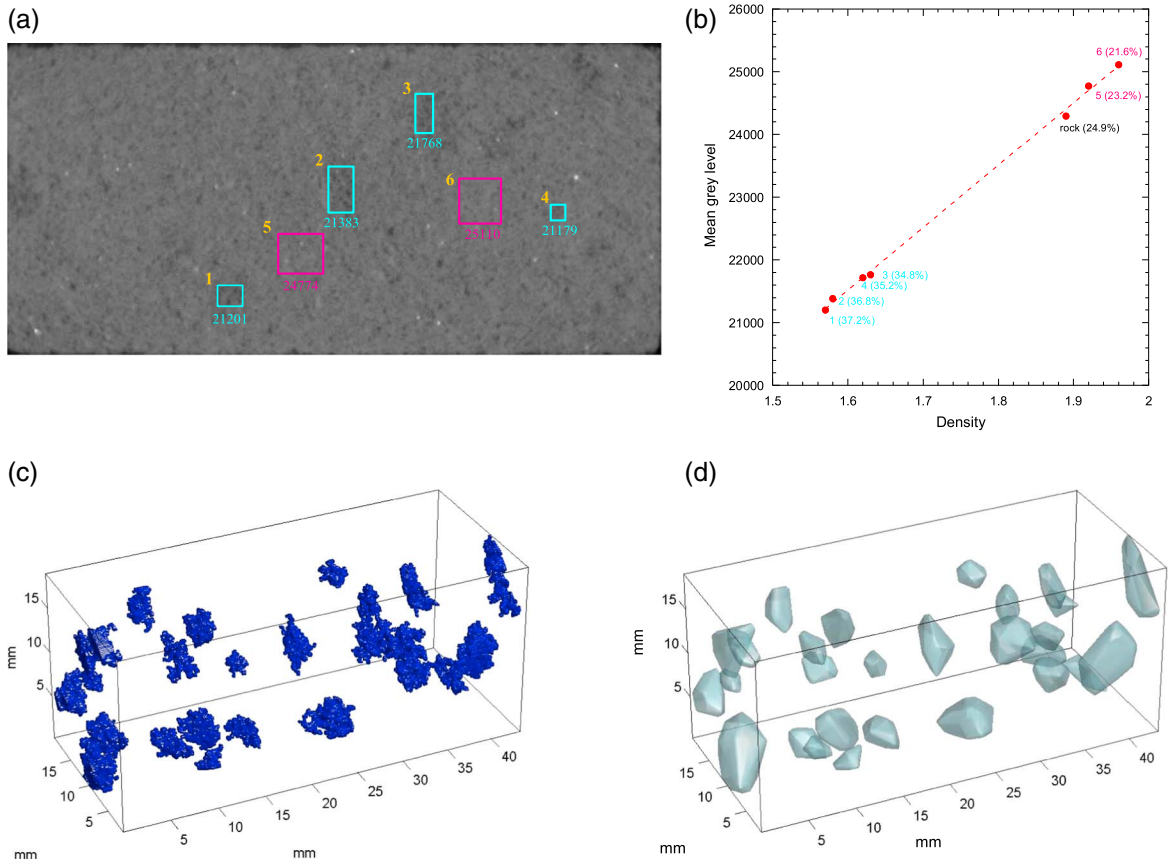

Figure 9. (a) CT image on intact Bleurswiller1 sandstone with resolution 49 μm. Several porosity clusters (dark) are visible in the CT image. The average porosity is given for each cluster using a calibration of the image (b) based of the mean grey levels for air and for the bulk value of the whole sample. (c) Three-dimensional view of binarized CT data to isolate the porosity patches (porosity greater than 39%) that are shown in blue. (d) Different 3-D view where the most porous voxels were enclosed with their convex hull (grey).

below remain relatively intact. The two other micrographs are from sample Bl24, showing two subparallel bands (Figure 13b) and two subparallel bands separated by a short distance without coalescence (Figure 13c).

4.3. Did Compaction Localization Nucleate From the Porosity Clusters?

To investigate the progressive development of compaction localization, the sample Bl28 was scanned at two different stages of deformation. In the first experiment it was triaxially loaded to just beyond the compactive yield stress C^*, retrieved and scanned. The sample was then loaded further to an axial strain of ~1.5% and scanned again (Figure 10). CT images for the deformed samples from these two experiments are denoted by Bl28a and Bl28b, respectively.

Unlike the image Bl28 acquired in the undeformed state, Bl28a and Bl28b do not indicate any porosity clusters of voxels with anomalously low grey levels, even though we meticulously scrutinized the images for such features. We characterized the spatial distribution of damage in the two images using the coefficient of variation as proxy. Whereas compaction bands could readily be identified in Bl28b, the other image Bl28a did not show any obvious signs of strain localization. From these observations we concluded that onset of shear-enhanced compaction at the critical stress C^* was associated with collapse of the porosity clusters. Furthermore, compaction bands did not develop until the stress level had increased significantly beyond C^*.

Fortin et al. [2006] performed a similar study using a medical scanner on a sample deformed to three different stages. They also observed that the porosity clusters had collapsed before the development of compaction bands and speculated that these bands might have nucleated by stress perturbations associated with collapse of the porosity clusters. Since their interpretation was based on 2-D projections of the CT images, the spatial relation between porosity clusters and compaction bands is somewhat ambiguous.

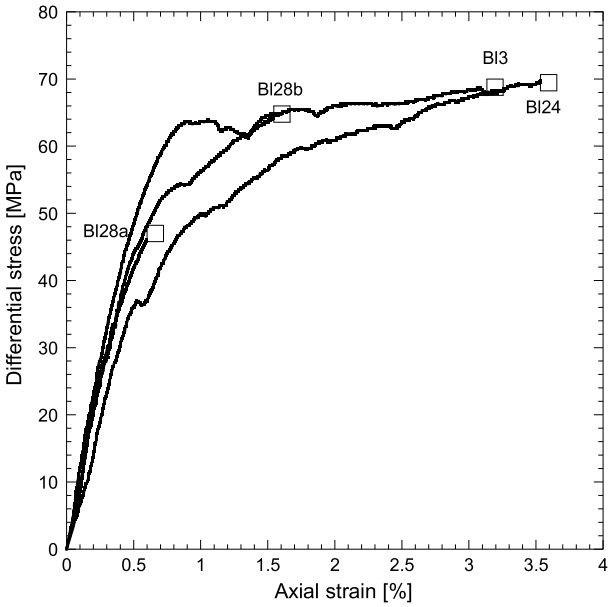

Figure 10. Differential stress versus axial strain for triaxial compression experiments on wet Bleurswiller1 sandstone. Samples Bl3 and Bl24 were deformed at effective pressures of 40 and 80 MPa. Bl28 was deformed at a confining pressure of 80 MPa to successively a maximum axial strain of ~0.5% and ~1.3%. These samples were subsequently studied using X-ray microCT after unloading.

The serial sections in Figure 14a illustrate the 3-D development of compaction bands in Bl28b, which seem to concentrate near the two ends of the sample. Compaction localization here is less intense in comparison to sample Bl24 (Figure 11), which was deformed to a significantly higher strain. As before, we binarized the Bl28b image using a threshold value of 0.5 for the normalized coefficient of variation (Figure 14b). To highlight the geometry and connectivity of the compaction bands, the intensely damaged voxels are shown in blue. Since we had mapped the spatial distribution of the preexisting porosity clusters in Bl28 (Figure 9d), we can assess the spatial relation between these clusters and the compaction bands by superposing the two binarized images (Figure 14c). Figure S3 presents a video that shows the superimposed binarized images rotating over 360°.

From a 3-D perspective, our superimposed images show that most of the porosity clusters and compaction bands seem unrelated. More than half of the porosity clusters are isolated from the compaction bands. There are also compaction bands that did not develop in the vicinity of any of the porosity clusters, and it seems unlikely that they had been nucleated by stress perturbation due to collapse of the clusters. If we were to project the CT images on a 2-D section, the clusters and bands would indicate an apparently stronger spatial correlation. The overall impression we have gained from a 3-D analysis of our CT images is that compaction

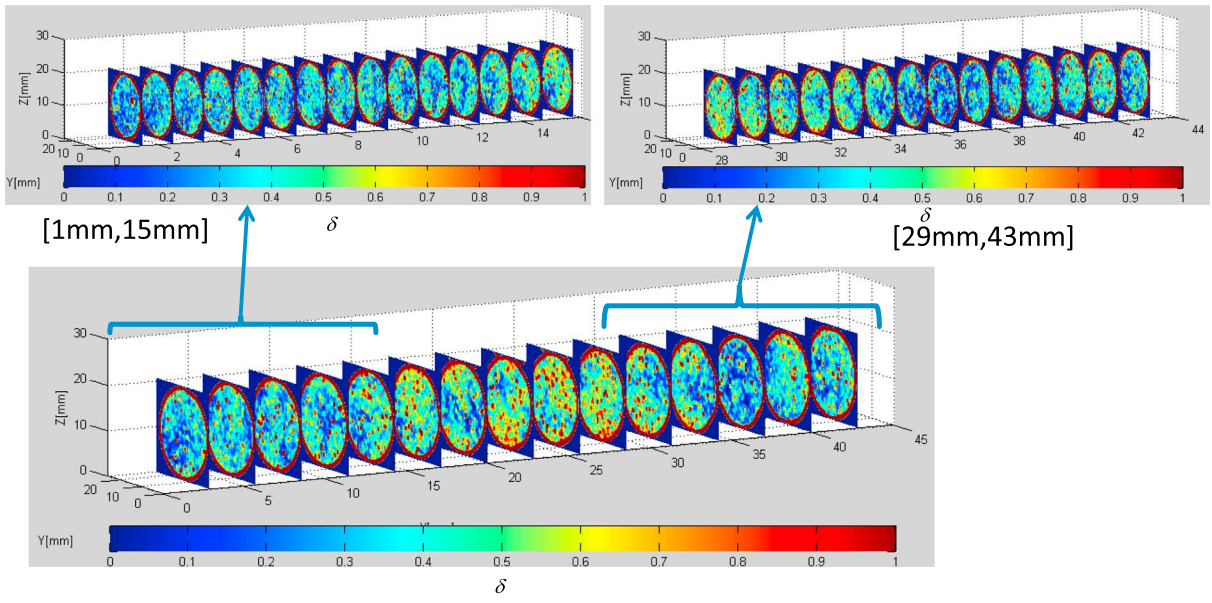

Figure 11. CT data on sample Bl24 of Bleurswiller1 deformed at an effective pressure of 80 MPa. The spatial distribution of the coefficient of variation δ is shown for selected serial sections orthogonal to the axes of the sample.

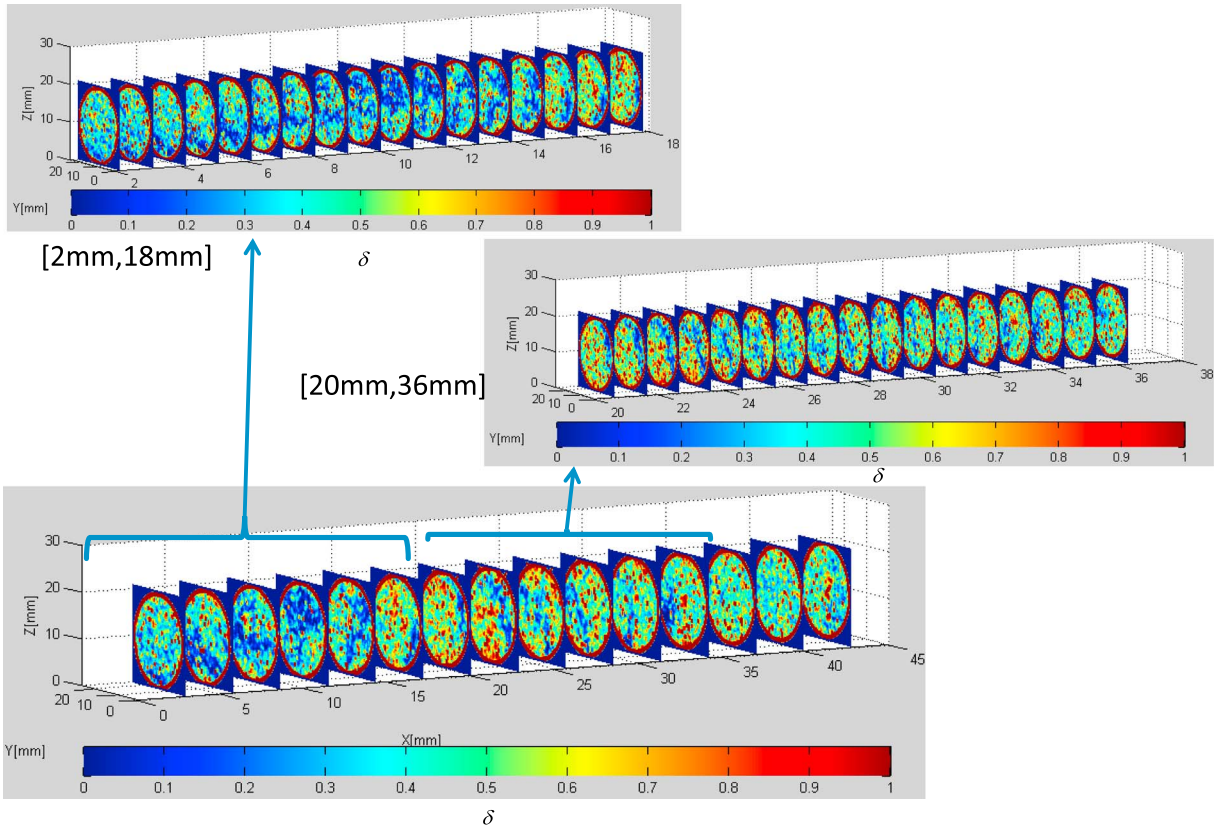

Figure 12. CT data on sample Bl3 of Bleurswiller1 deformed at an effective pressure of 40 MPa. The spatial distribution of the coefficient of variation δ is shown for selected serial sections orthogonal to the axes of the sample.

localization in sample Bl28 have not nucleated from collapse of the porosity clusters, and indeed, the two phenomena may not have any casual relation to one another.

Our SEM observations on the failed samples also support this conclusion. We were able to identify many compact areas with poorly sorted grains that appear to be collapsed porosity clusters (Figures 15a and 15b). Even though a number of compaction bands have developed in these samples, they were not located in the vicinity of these collapsed clusters. Whereas the well-sorted grains in the compaction bands have undergone significant comminution, grain damage is relatively minor in the collapsed clusters.

5. Discussion

5.1. Compactive Yield and Linear Cap

We have conducted a comprehensive investigation of the mechanical deformation and failure mode of Bleurswiller sandstone over a broad range of confining and pore pressures. With increasing confinement, the failure mode undergoes a transition from brittle faulting to cataclastic flow that may localize in the form of shear and/or compaction bands (Figure 5). Data for the brittle strength as a function of confining pressure fall on a linear Coulomb envelope. Interestingly, the compactive yield stress C^* for the onset of shear-enhanced compaction can be described by a cap that is also linear (Figures 2 and 4). This latter observation is considered to be anomalous. In a recent review of mechanical compaction behaviors in 10 sandstones (with porosities ranging from 13% to 35%), *Wong and Baud* [2012] concluded that they all have elliptical caps, Bleurswiller sandstone being the sole exception. Elliptical caps were also documented in recent studies of poorly lithified sandstone and sand [*Skurtveit et al*., 2013; *Nguyen et al*., 2014].

Previous mechanical investigations of Bleurswiller sandstone [*Fortin et al*., 2006; *Tembe et al*., 2008; *Cheung et al*., 2012] were on water-saturated samples of a block that contains relatively high clay content. In this study we deformed dry samples from the same block, and our compactive yield data also fall on a cap that is relatively

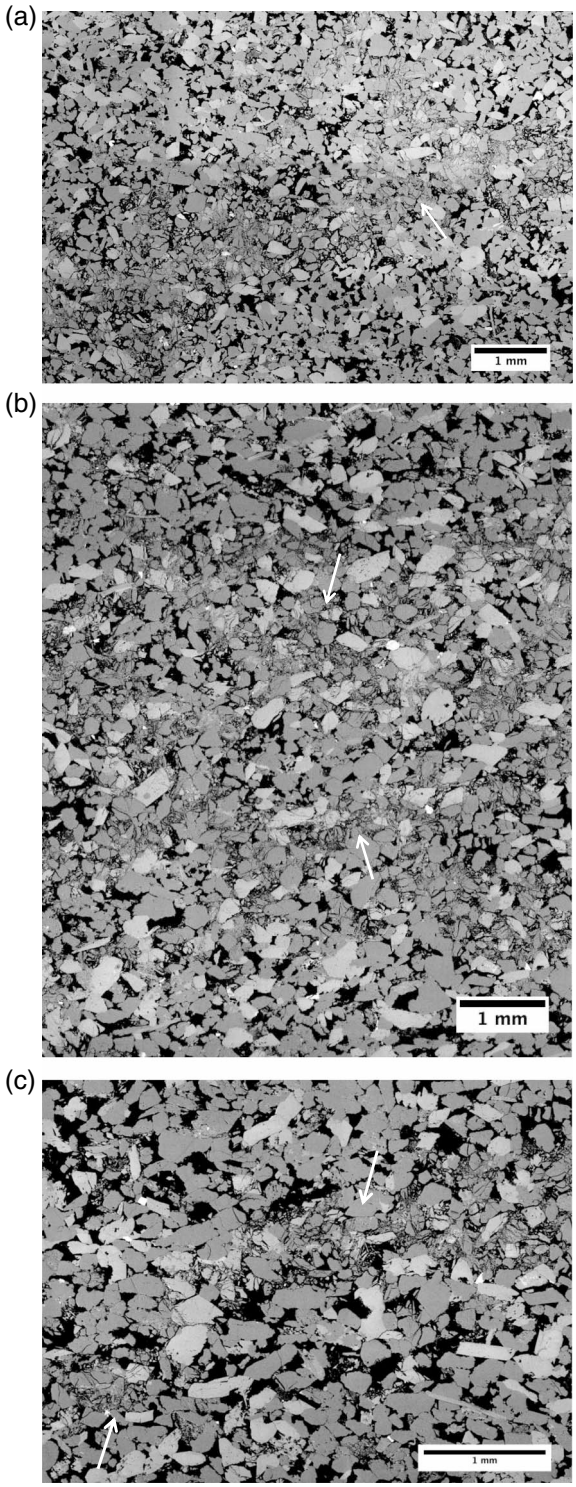

Figure 13. Backscattered SEM images of deformed samples of Bleurswiller1 showing (a) a compaction band of about 1 mm of thickness in sample Bl3 deformed at an effective pressure of 40 MPa, (b) two subparallel compaction bands, and (c) two very close compaction bands in sample Bl24 deformed at an effective pressure of 80 MPa. Compaction bands are indicated by a white arrow on each micrograph.

linear (Figure 2). Furthermore, we here investigated another block of Bleurswiller sandstone that contains relatively little clay, with quartz and feldspar contents similar to Diemelstadt sandstone, which has an elliptic cap and can fail by compaction band formation [*Louis et al.*, 2006]. Since compactive yield data for our Bleurswiller2 samples also fall on a relatively linear cap (Figure 4b), we can rule out either mineralogy or presence of water as important factors for the discrepancy with most porous sandstones in the shape of the cap, and the anomalously linear behavior of Bleurswiller sandstone is mostly likely related to its pore structure.

5.2. Effect of Water on Mechanical Failure

We have conducted experiments to investigate both the chemical and mechanical effects of water in failure. Related to the former effect, our data (Figures 2 and 4) show significant weakening of Bleurswiller sandstone in the presence of water. This phenomenon of water weakening was observed in both the brittle faulting and cataclastic flow regimes, in basic agreement with the observation of *Baud et al.* [2000] for four sandstones with nominal porosities ranging from 11% to 35 %. They reported that the compactive yield strengths in the water-saturated samples were lower than those in the dry samples deformed under comparable pressure conditions by 20–70%, whereas the reductions of brittle strength in the presence of water fell in the range of 5–17%. The observed relation between water weakening and failure mode can be explained by a reduction of specific surface energy in the presence of water. The ratio λ between the specific energy values in the presence of water and in vacuo was observed to be less than 1. *Baud et al.* [2000] adopted the Hertzian fracture and damage mechanics models in the cataclastic flow and brittle faulting regimes, respectively, to predict that the initial yield stress C^* would scale as $\lambda^{3/2}$, and the uniaxial compressive strength as $\lambda^{1/2}$.

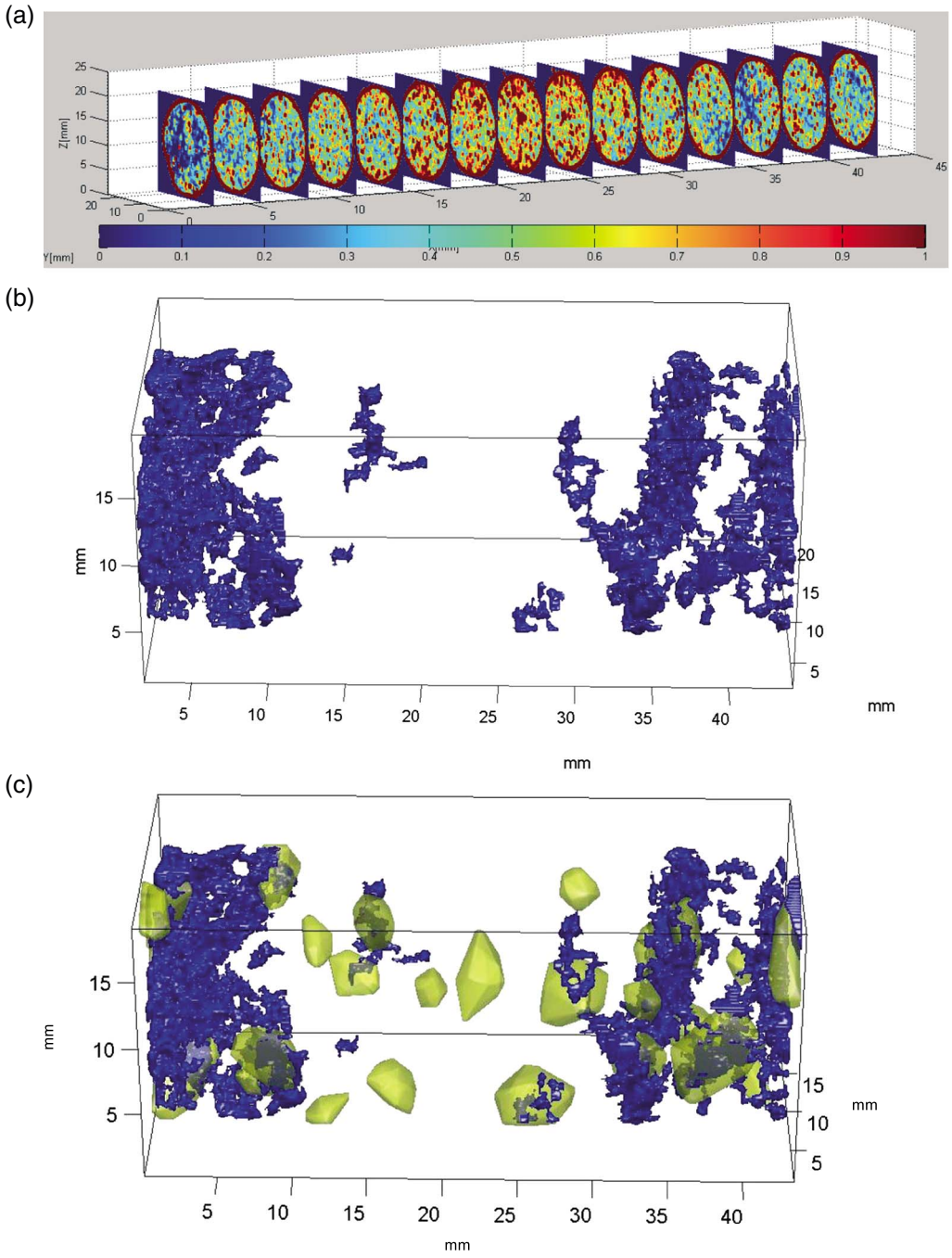

Figure 14. CT data on sample Bl28b of Bleurswiller1 deformed at an effective pressure of 80 MPa. (a) The spatial distribution of the coefficient of variation δ is shown for selected serial sections orthogonal to the axes of the sample. (b) Binarized data for the normalized coefficient of variation. Compaction bands (intensely damaged voxels) are shown in blue. (c) Superimposition of convex porosity hulls (yellow) and compaction bands (blue) demonstrates that there is no clear association between the collapsed porosity clusters and nucleation of compaction bands by stress perturbations. Parts of the compaction bands that appear black are seen through the convex porosity hulls.

Adopting this model and following a procedure identical to that of *Baud et al.* [2000], for Bleurswiller2 we inferred $\lambda = 0.80$ and $\lambda = 0.77$ from our P^* and brittle strength data, respectively. Similarly, we infer from the P^* data of *Tembe et al.* [2008] a value of $\lambda = 0.75$ for Bleurswiller1. They inferred that values of λ are in the range of the highest values reported for other sandstones. This is not unexpected since *Baud et al.* [2000] observed an overall trend for the water-weakening effect to be more pronounced in feldspar-rich sandstone. The

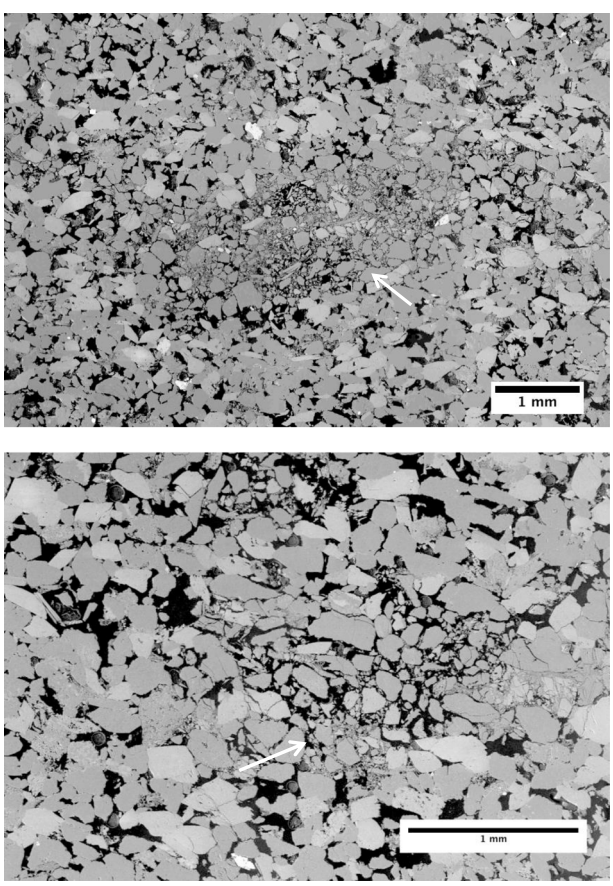

Figure 15. Backscattered SEM images showing the collapse of porosity patches in samples of Bleurswiller1 (a) Bl28b and (b) Bl3 deformed at effective pressures of 80 MPa and 40 MPa, respectively. The collapsed patches are indicated by a white arrow on each micrograph. No compaction bands are visible in the vicinity of the collapsed patches.

more pronounced effect observed on Bleurswiller1 is also consistent with the significantly higher proportion of clay in this block.

As for the mechanical effect of pore fluid, there is a paucity of data on cataclastic flow. Our study is one of the first to systematically investigate this aspect of the compactive yield behavior, and our data suggest a α value very close to but less than 1 for the compactive yield stress C* of Bleurswiller sandstone (Figure 3). In contrast, the effective stress behavior of elastic deformation and brittle failure has been extensively investigated. For elastic deformation, the effective stress law can be derived from the theory of linear poroelasticity [*Berryman*, 1992; *Wang*, 2000], with an effective stress coefficient given by the Biot-Willis coefficient, which has a value between 0 and 1. *Paterson and Wong* [2005] provided a comprehensive compilation of experimental data for this coefficient. They also reviewed the literature related to brittle failure and concluded that the considerable body of experimental work has shown that to a fairly good approximation, Terzaghi's effective stress rule governs the brittle faulting behavior of a wide variety of rocks, with an effective stress coefficient α equal to 1.

However, our brittle fracture data here (Figure 3) indicate a α value close to but less than 1 for Bleurswiller sandstone. It should be noted since most investigations of the effective stress behavior were performed over a pore pressure range much smaller than ours, they might not be able to resolve the somewhat small difference noted here. As noted by *Paterson and Wong* [2005], because the micromechanical basis for the effective stress behavior remains unclear, much controversy and confusion have persisted regarding the effective stress law for brittle failure. Our observations are in agreement with *Robin* [1973] who postulate that since fracture strength is sensitively dependent on the opening or closing of microcracks, its effective stress behavior is likely governed by how pore volume changes in response to the mean stress and pore pressure. According to linear poroelasticity [*Berryman*, 1992; *Wang*, 2000], the effective stress coefficient pertinent to pore volumetric strain is given by

$$\alpha = 1 - \frac{\phi}{K_s(1/K - 1/K_s)} \tag{1}$$

where ϕ is the porosity, K is the bulk modulus of the porous rock, and K_s is the bulk modulus of the solid grains. In a cracked solid, one expects $K_s \gg K$, and therefore, the second term on the right-hand side can be very small. Accordingly, the effective stress coefficient is predicted to have a value close to but slightly less than 1.

5.3. Pore Space Heterogeneity and Strain Localization

Synthesizing observations from CT imaging in 3-D and SEM, we have clarified the influence of the porosity clusters on mechanical compaction and strain localization in Bleurswiller sandstone. In a porous sandstone

with a relatively homogeneous pore space, the onset of shear-enhanced compaction is associated with initiation of Hertzian fractures at grain contacts [*Wong et al*., 1997]. In contrast, our observations have shown that the onset in Bleurswiller sandstone is intimately related to the collapse of porosity clusters, and Hertzian fracturing would not develop until further increase of stress.

From a 3-D perspective, our CT observations on a sample deformed to different stages strongly suggest that collapse of the porosity clusters and development of compaction bands are unrelated. Our microstructural observations using the SEM corroborate this conclusion. This contradicts the hypothesis of *Fortin et al*. [2006] (based on *AE* mapping and CT observation in 2-D) that compaction localization in Bleurswiller sandstone may nucleate from collapse of the porosity clusters. Although the porosity clusters have minimal impact on compaction band initiation, it should be noted that they may have significant influence on the geometric attributes of discrete compaction band. Our SEM observations have shown that the grains in a cluster are poorly sorted, and both theoretical [*Wang et al*., 2008] and microstructural [*Cheung et al*., 2012] observations suggest that compaction localization would be inhibited in such an assembly. Once nucleated, a compaction band tends to follow a relatively tortuous path so as to avoid passing through the porosity clusters. Accordingly, the compaction bands in Bleurswiller sandstone appear to be more diffuse and tortuous in comparison to those in Bentheim and Diemelstadt sandstones.

5.4. Collapse of Porosity Cluster: A Micromechanical Model for the Linear Cap

A micromechanical model for the initiation of shear-enhanced compaction in Bleurswiller sandstone should take into account these two aspects highlighted in our study: critical role of the collapse of porosity clusters, and the robust observation of compactive yield caps that are approximately linear. To our knowledge there are two recent models that predict such a linear cap in a porous rock. The first was proposed by *Guéguen and Fortin* [2013], who considered a periodic grain network in 2-D and assumed the predominate mechanism to be grain crushing. Initial yield occurs when the stress field at a grain contact attains the threshold for Hertzian fracture, and the model predicts that the macroscopic yield stresses (differential stress Q and effective mean stress P) are linearly related, with a slope of -2.3. This model seems unlikely to apply here for two reasons. First, our observations indicate that Hertzian fracture and grain crushing were not involved during the onset stage, and they become important only well after initial yielding. Second, the predicted slope of -2.3 is significantly steeper than the slopes (~ -1) of the experimentally determined linear caps.

A second model is the pore collapse model analyzed by *Zhu et al*. [2010]. If the porosity cluster can be idealized as a spherical pore embedded in a matrix that fails according to the Coulomb criterion, then this model predicts that onset of pore collapse occurs when the stress field in the vicinity of pore attains the threshold according to the Coulomb criterion, such that the macroscopic stresses at the initial yield point C^* are linearly related according to

$$Q = \frac{3(7-5\upsilon)}{10(2-\upsilon)}(P^* - P) \tag{2}$$

where υ denotes Poisson's ratio and P^* is the critical effective pressure at the onset of pore collapse. Interestingly, the predicted linear cap does not depend on the Coulomb failure parameters, and it has a slope with magnitude that falls in a relatively narrow range between 0.9 and 1.05, corresponding to values of υ between 0 and 0.5. For comparison with the Bleurswiller1 data, we have plotted in Figure 2 a straight line with an intermediate slope of -0.95. As for Bleurswiller2, since the cap is somewhat steeper, for comparison we have plotted in Figure 4 the straight line with the steepest slope of -1.05 as predicted by the pore collapse model. Notwithstanding, the idealized assumptions in the micromechanical model, it captures the important role of porosity clusters, and the agreement between model prediction and experimental data (for dry and wet tests on two different blocks) is quite reasonable.

For samples that underwent shear-enhanced compaction, the data for effective mean stress versus porosity can typically be separated into two stages: initially after C^* the curve is approximately linear, followed by a second stage with progressively decreasing slope (Figure 16a). An analogous separation can be made on the hydrostatic data (Figure 16b). Our microstructural observations indicate that the initial linear stage corresponds to the progressive collapse of all the porosity clusters, and transition between the initial and second stages approximately corresponds to the onset of Hertzian fracture. We selected a subset of data for saturated Bleurswiller1 samples with the two stages beyond C^* sufficiently well defined, such that the second

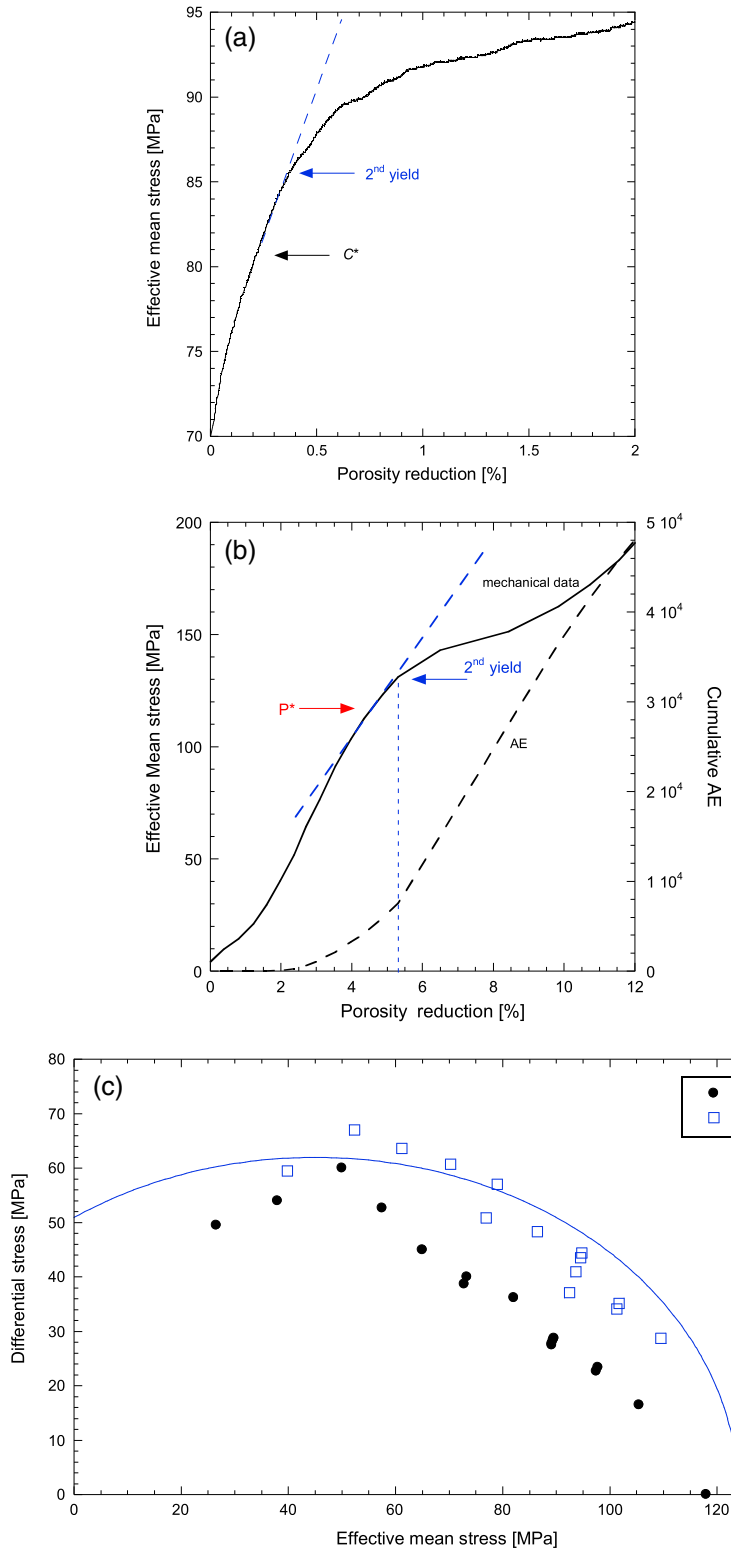

Figure 16. (a) Mechanical data for an experiment performed on the sample of Bleurswiller1 (Bl23) at an effective pressure of 70 MPa. The onset of shear-enhanced compaction C* and a second yield point, corresponding to the collapse of the porosity clusters and the onset of Hertzian fracture, are shown. (b) Mechanical data and cumulative acoustic emission for a hydrostatic performed on Bleurswiller1 (sample Bl19). *P** and the second yield point are also indicated. (c) *C** and the second yield point are shown in the stress space (*P*-*Q*). The second yield envelope can be described in a first approximation as an elliptical cap.

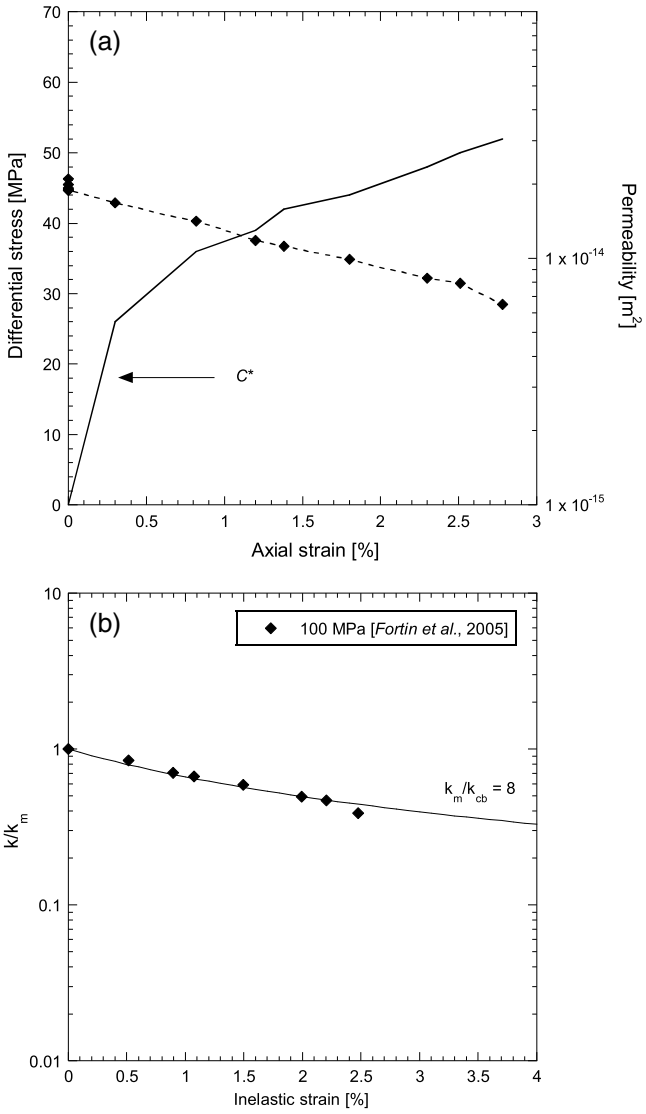

Figure 17. (a) Differential stress and permeability as a function of axial strain for a triaxial permeability experiments performed on a Bleurswiller1 sandstone sample at an effective pressure of 100 MPa [*Fortin et al.*, 2005]. (b) Normalized permeability as a function of inelastic strain for the same experiment. The solid lines represent the predictions of equation (4) for the permeability contrast k_m/k_{cb} indicated.

yield points can be picked. Since there is a certain ambiguity related to our picks of these critical stresses, the data are somewhat scattered, but overall they define a subsequent yield envelope which is nonlinear, and to a first approximation, can be described as an elliptical cap (Figure 16c), analogous to the observations in most porous sandstones with initial yield related to Hertzian fracture and grain crushing [*Wong and Baud*, 2012].

5.5. Evolution of Permeability With Compaction Band Formation

The number of compaction bands in each deformed sample is approximately linearly correlated with the amount of accumulated inelastic axial strain (Figure 6), in agreement with previous literature [e.g., *Baud et al.*, 2012]:

$$\varepsilon_p = \varepsilon_0 + \beta.n \tag{3}$$

With $\varepsilon_0 = 4.6 \times 10^{-3}$ and $\beta = 3.34 \times 10^{-3}$, where ε_0 is the inelastic strain necessary to trigger the first band in the sample and β is the inelastic strain necessary to propagate each additional band.

The local porosity reduction within a compaction band β' can be simply estimated from the macroscopic inelastic strain β (taken over the full length of the sample = 40 mm) divided by the band thickness *l*. Our microstructural observations showed that on average $l = 0.95$ mm, which gives a porosity reduction in the band of $\beta' = 14.3\%$, in almost perfect agreement with previously inferred values for Bentheim and Diemelstadt sandstones [*Vajdova et al.*, 2004; *Baud et al.*, 2012].

Motivated by their microstructural observations regarding compaction band formation in Bentheim sandstone, *Vajdova et al.* [2004] formulated a model for the permeability reduction in term of a layered medium with significant permeability contrast between the discrete bands and matrix. The effective permeability of such a tabular medium can be expressed as

$$k = \frac{k_m}{\left(\frac{\varepsilon_p}{\beta'}\right)\left(\frac{k_m}{k_{cb}} - 1\right) + 1} \tag{4}$$

where k_m and k_{cb} are the permeability of the matrix and of the bands, respectively. Recently *Baud et al.* [2012] concluded that the same model applies to Diemelstadt sandstone. The permeability contrast between the bands and the matrix was found to be between 2 and 3 orders of magnitude. The consistency between the porosity reductions inferred in the compaction bands for the three studied sandstone would a priori suggest a comparable permeability contrast in Bleurswiller sandstone. We applied the same model to

Fortin et al., 2005 permeability data for $P_{eff} = 100$ MPa (Figure 17a), combining equations (3) and (4), and taking into account the size difference between our samples and those of this earlier study. The very low permeability contrast inferred in this case (Figure 17b) is in fact consistent with our CT data and microstructural observations for Bleurswiller sandstone and emphasizes that the geometry of compaction bands has further implication on fluid flow properties. The compaction bands formed in Bentheim and Diemelstadt sandstone are more continuous tabular structures, acting as efficient permeability barriers [*Vajdova et al.*, 2004; *Baud et al.*, 2012]. In contrast, compaction bands in Bleurswiller sandstone are much more inclined and lack of connectivity in 3-D, having less impact on permeability. In the most homogeneous sandstones, tabular continuous bands can efficiently impact fluid flow, whereas local heterogeneities make the bands more tortuous, less continuous, and in turn less efficient as permeability barrier. Recent permeability measurements on natural compaction bands by *Deng et al.* [2015] and numerical simulations based on CT imaging [*Sun et al.*, 2011] also support the idea that the impact of compaction bands on fluid flow should be evaluated case by case and that their distribution and geometric attributes should be characterized.

6. Conclusion

On the basis of our systematic investigation of mechanical failure and strain localization in Bleurswiller sandstone using rock mechanics testing, X-ray CT imaging, and microstructural observations, we have arrived at a number of conclusions.

1. With increasing confinement, the failure mode undergoes a transition from brittle faulting to cataclastic flow that may localize in the form of shear and/or compaction bands. The brittle strength data map out a linear Coulomb envelope. The compactive yield stress for the onset of shear-enhanced compaction fall on a cap that is also linear.
2. Our data for saturated samples deformed over a broad range of pore pressure show that the effective pressure principle can be applied in both the brittle faulting and cataclastic flow regimes, with effective pressure coefficients close to but somewhat less than 1.
3. Comparison of dry and wet data reveals a significant weakening effect of water in both deformation regimes, which can be interpreted by a micromechanical model that takes into account reduction of the specific surface energy in the presence of water.
4. The CT and microstructural observations indicate that the linear yield caps are likely related to collapse of the preexisting porosity clusters. It is demonstrated that the caps and their slopes are in agreement with a micromechanical model based on the collapse of a spherical pore embedded in an elastic-plastic matrix that obeys the Coulomb failure criterion.
5. Synthesis of the CT and microstructural data indicates that there is no casual relation between collapse of the porosity clusters and nucleation of the compaction bands. Instead, the collapsed porosity clusters may act as barriers for the propagation of compaction localization, rendering the compaction bands to propagate along relatively tortuous and diffuse paths. This in turn results in permeability reduction that is significantly lower than that associated with compaction band formation in other porous sandstones.

Acknowledgments

Data will be available on demand. We thank Peter Eichhubl, Harald Milsch, and the Associate Editor for thoughtful reviews. We are grateful to Jérôme Fortin for providing the block of Bleurswiller1 and to Jean-Daniel Bernard for helping with some of the experiments. We have benefited from discussions with Mike Heap, Laurent Louis, and Alexandra Rolland. This work was partially funded by the NSF of China (41404145) and the Basic Scientific Funding of Chinese National Nonprofit Institutes (IGCEA1415). The research at Stony Brook was partially supported by the Office of Basic Energy Sciences, Department of Energy under grant DE-FG02-10ER16159. The research at Strasbourg and Hong Kong were partially funded by the France-Hong-Kong Collaborative Program Procore 30805PM and F-CUHK406/13, respectively.

References

Baud, P., W. Zhu, and T.-f. Wong (2000), Failure mode and weakening effect of water on sandstone, *J. Geophys. Res.*, *105*, 16,371–16,390, doi:10.1029/2000JB900087.

Baud, P., E. Klein, and T.-f. Wong (2004), Compaction localization in porous sandstones: Spatial evolution of damage and acoustic emission activity, *J. Struct. Geol.*, *26*, 603–624.

Baud, P., S. Vinciguerra, C. David, A. Cavallo, E. Walker, and T. Reuschlé (2009), Compaction and failure in high porosity carbonates: Mechanical data and microstructural observations, *Pure Appl. Geophys.*, *166*, 869–898.

Baud, P., P. G. Meredith, and E. Townend (2012), Permeability evolution during triaxial compaction of an anisotropic porous sandstone, *J. Geophys. Res.*, *117*, B05203, doi:10.1029/2012JB009176.

Berryman, J. G. (1992), Effective stress for transport properties of inhomogeneous rocks, *J. Geophys. Res.*, *97*(B12), 17,409–17,424, doi:10.1029/92JB01593.

Brace, W. F., and R. J. Martin (1968), A test of the law of effective stress for crystalline rocks of low porosity, *Int. J. Rock Mech. Min. Sci.*, *5*, 415–436.

Charalampidou, E.-M., S. A. Hall, S. Stanchits, H. Lewis, and G. Viggiani (2011), Characterization of shear and compaction bands in a porous sandstone deformed under triaxial compression, *Tectonophysics*, *503*, 8–17.

Charalampidou, E.-M., S. A. Hall, S. Stanchits, G. Viggiani, and H. Lewis (2013), Shear-enhanced compaction band identification at the laboratory scale using acoustic and full-field methods, *Int. J. Rock Min. Sci.*, *67*, 240–252.

Cheung, C., P. Baud, and T.-f. Wong (2012), Effect of grain size distribution on the development of compaction localization in porous sandstone, *Geophys. Res. Lett.*, *39*, L21302, doi:10.1029/2012GL053739.
Deng, S., L. Zuo, A. Aydin, J. Dvorkin, and T. Murkerji (2015), Permeability characterization of natural compaction bands using core flooding experiments and three-dimensional image-based analysis: Comparing and contrasting the results from two different methods, *AAPG Bull.*, *99*(1), 27–49.
Eichhubl, P., J. N. Hooker, and S. E. Laubach (2010), Pure and shear-enhanced compaction bands in Aztec Sandstone, *J. Struct. Geol.*, *32*, 1873–1886.
Fortin, J., A. Schubnel, and Y. Guéguen (2005), Elastic wave velocities and permeability evolution during compaction of Bleurswiller sandstone, *Int. J. Rock Mech. Min. Sci.*, *42*, 873–889.
Fortin, J., S. Stanchits, G. Dresen, and Y. Guéguen (2006), Acoustic emission and velocities associated with the formation of compaction bands in sandstone, *J. Geophys. Res.*, *111*, B10203, doi:10.1029/2005JB003854.
Fossen, H., R. A. Schultz, and A. Torabi (2011), Conditions and implications for compaction band formation in the Navajo sandstone, Utah, *J. Struct. Geol.*, *33*, 1477–1490.
Gonzalez, R. C., and R. E. Woods (2008), *Digital Image Processing*, 3rd ed., Prentice Hall, New York.
Guéguen, Y., and J. Fortin (2013), Elastic envelopes of porous sandstones, *Geophys. Res. Lett.*, *40*, 3550–3555, doi:10.1002/grl.50676.
Heap, M. J., N. Brantut, P. Baud, and P. G. Meredith (2015), Time-dependent compaction band formation in sandstone, *J. Geophys. Res. Solid Earth*, *120*, doi:10.1002/2015JB012022.
Hill, R. E. (1989), Analysis of deformation bands in the Valley of Fire State Park, Nevada, MS thesis, 68 pp., Univ. of Nevada, Las Vegas.
Holcomb, D. J., and W. A. Olsson (2003), Compaction localization and fluid flow, *J. Geophys. Res.*, *108*(B6), 2290, doi:10.1029/2001JB000813.
Kampfer, G., and Y. M. Leroy (2009), Imperfection and burial-depth sensitivity of the initiation and development of kink folds in laminated rocks, *J. Mech. Phys. Sol.*, *57*(8), 1314–1339.
Ketcham, R. A., and W. D. Carlson (2001), Acquisition, optimization and interpretation of X-ray computed tomographic imagery: Applications to the geosciences, *Comp. Geosci.*, *27*, 381–400.
Klein, E., P. Baud, T. Reuschlé, and T.-f. Wong (2001), Mechanical behaviour and failure mode of Bentheim sandstone under triaxial compression, *Phys. Chem. Earth (A)*, *26*, 21–25.
Louis, L., T.-f. Wong, P. Baud, and S. Tembe (2006), Imaging strain localization by X-ray computed tomography: Discrete compaction bands in Diemelstadt sandstone, *J. Struct. Geol.*, *28*, 762–775.
Maillot, B., and Y. M. Leroy (2006), Kink-fold onset and development based on maximum strength theorem, *J. Mech. Phys. Sol.*, *54*, 2030–2059.
Mollema, P. N., and M. A. Antonellini (1996), Compaction bands: A structural analog for anti-mode I cracks in Aeolian sandstone, *Tectonophysics*, *267*, 209–228.
Nguyen, V. H., N. Gland, J. Dautriat, C. David, J. Wassermann, and J. Guelard (2014), Compaction, permeability evolution and stress path effects in unconsolidated sand and weakly consolidated sandstone, *Int. J. Rock Mech. Min. Sci.*, *67*, 226–239.
Otani, J., T. Mukunoki, and K. Sugawara (2005), Evaluation of particle crushing in soils using X-ray CT data, *Soils Found.*, *45*, 99–108.
Paterson, M. S., and T.-f. Wong (2005), *Experimental Rock Deformation—The Brittle Field*, 2nd ed., Springer, New York.
Robin, P. Y. F. (1973), Note on effective pressure, *J. Geophys. Res.*, *78*, 2434–2437, doi:10.1029/JB078i014p02434.
Schultz, R. A., C. H. Okubo, and H. Fossen (2010), Porosity and grain size controls on compaction band formation in Jurassic Navajo sandstone, *Geophys. Res. Lett.*, *37*, L22306, doi:10.1029/2010GL044909.
Skurtveit, E., A. Torabi, R. H. Gabrielsen, and M. D. Zoback (2013), Experimental investigation of deformation mechanisms during shear-enhanced compaction in poorly lithified sandstone and sand, *J. Geophys. Res. Solid Earth*, *118*, 4083–4100, doi:10.1002/jgrb.50342.
Sternlof, K. R., J. W. Rudnicki, and D. D. Pollard (2005), Anticrack-inclusion model for compaction bands in sandstone, *J. Geophys. Res.*, *110*, B11403, doi:10.1029/2005JB003764.
Sun, W., J. W. Rudnicki, J. E. Andrade, and P. Eichhubl (2011), Connecting microstructural attributes and permeability from 3D tomographic images of in situ shear-enhanced compaction bands using multiscale computations, *Geophys. Res. Lett.*, *38*, L10302, doi:10.1029/2011GL047683.
Tembe, S., P. Baud, and T.-f. Wong (2008), Stress conditions for the propagation of discrete compaction bands in porous sandstone, *J. Geophys. Res.*, *113*, B09409, doi:10.1029/2007JB005439.
Townend, E., B. D. Thompson, P. M. Benson, P. G. Meredith, P. Baud, and R. P. Young (2008), Imaging compaction band propagation in Diemelstadt sandstone using acoustic emission locations, *Geophys. Res. Lett.*, *35*, L15301, doi:10.1029/2008GL034723.
Vajdova, V., P. Baud, and T.-f. Wong (2004), Permeability evolution during localized deformation in Bentheim sandstone, *J. Geophys. Res.*, *109*, B10406, doi:10.1029/2003JB002942.
Wang, B., Y. Chen, and T.-f. Wong (2008), A discrete element model for the development of compaction localization in granular rock, *J. Geophys. Res.*, *113*, B03202, doi:10.1029/2006JB004501.
Wang, H. F. (2000), *Theory of Linear Poroelasticity With Applications to Geomechanics and Hydrogeology*, Princeton Univ. Press, Princeton, N. J.
Wong, T.-f., and P. Baud (2012), The brittle-ductile transition in rocks: A review, *J. Struct. Geol.*, *44*, 25–53.
Wong, T.-f., C. David, and W. Zhu (1997), The transition from brittle faulting to cataclastic flow in porous sandstones: Mechanical deformation, *J. Geophys. Res.*, *102*, 3009–3025, doi:10.1029/96JB03281.
Wong, T.-f., P. Baud, and E. Klein (2001), Localized failure modes in a compactant porous rock, *Geophys. Res. Lett.*, *28*, 2521–2524, doi:10.1029/2001GL012960.
Zhang, J., T.-f. Wong, and D. M. Davis (1990), Micromechanics of pressure-induced grain crushing in porous rocks, *J. Geophys. Res.*, *95*, 341–352, doi:10.1029/JB095iB01p00341.
Zhu, W., P. Baud, and T.-f. Wong (2010), Micromechanics of cataclastic pore collapse in limestone, *J. Geophys. Res.*, *115*, B04405, doi:10.1029/2009JB006610.